Article   https://doi.org/10.1038/s41467-025-63115-9

Biomimetic microstructure design for ultrasensitive piezoionic mechanoreceptors in multimodal object recognition

Check for updates

Mingqi Ding[1,9], Pengshan Xie[1,9], Jingwen Wang[2,3,9], Wu Guo[4], Haifan Li[5], Siliang Hu[1], Dengji Li [1], Bowen Li [1,6], Nan Wang[1], Chun-Yuen Wong [5], Jia Sun [2,3] ✉ & Johnny C. Ho [1,6,7,8] ✉

The challenge of achieving high recognition accuracy in artificial mechanoreceptors arises from the trade-off between sensitivity and stability in the sensing unit. Inspired by human skin, we developed a biomimetic approach that involves structural and engineering enhancements for ionic-conducting polyvinyl alcohol/$Ti_3C_2T_x$ (PVA/MXene) composite hydrogel microneedles (HM) to enhance the sensitivity. By integrating the HM with a polyethylene terephthalate/indium tin oxide (PET/ITO) film, we create a non-faradaic junction that ensures stable electrical output without transmission loss under stimulation. Furthermore, the significant alteration in nanosheet spacing facilitates proton transport along the MXene microchannels, increasing the plasmonic gradient between the junction and the hydrogel's center, thereby boosting piezoionic efficiency. Consequently, the biomimetic sensing unit achieves a high power density of 165.6 mW m^{-2} and exceptional sensing stability over 10,000 cycles. When combined with vertical memristor units, this system effectively captures and transforms characteristic signals from various objects, achieving a recognition accuracy of 90%.

Artificial tactile neuromorphic devices, or mechanoreceptors, inspired by brain-like non-von Neumann architectures, have been developed for diverse human-machine interaction applications, such as health monitoring, virtual reality, and object recognition[1–3]. Despite advancements in stretchability and integration, achieving high recognition accuracy remains a significant challenge for electronic skins (e-skins) and wearable electronics[4,5]. While these devices can effectively differentiate essential characteristics like hardness, texture, and size, they often falter in precise tasks, such as accurately delivering a baseball or real-time heartbeat monitoring. Typically,

mechanoreceptors combine a mechanical sensing unit with a neuromorphic computing unit, where high mechanical-electrical conversion efficiency and sensitivity are crucial for detecting weak stresses and recognizing object morphologies[6,7]. However, due to the rigidity of electronic conductors and thermally activated electron-hopping, the trade-off between sensitivity and stability poses a major obstacle to improving recognition accuracy.

Ionic hydrogels have attracted significant attention for their flexibility, reconfigurability, adhesiveness, and cell-like ion channels[8,9]. By designing a non-faradaic junction (NFJ) at the hydrogel/electrode

[1]Department of Materials Science and Engineering, City University of Hong Kong, Kowloon, Hong Kong, China. [2]Hunan Key Laboratory for Super-microstructure and Ultrafast Process, School of Physics, Central South University, Changsha, Hunan, China. [3]State Key Laboratory of Transducer Technology, Shanghai Institute of Microsystem and Information Technology, Shanghai, China. [4]National Key Laboratory of Advanced Polymer Materials, Polymer Research Institute of Sichuan University, Chengdu, China. [5]Department of Chemistry, City University of Hong Kong, Kowloon, Hong Kong, China. [6]Shenzhen Research Institute, City University of Hong Kong, Shenzhen, China. [7]State Key Laboratory of Terahertz and Millimeter Waves, City University of Hong Kong, Hong Kong SAR, China. [8]Institute for Materials Chemistry and Engineering, Kyushu University, Fukuoka, Japan. [9]These authors contributed equally: Mingqi Ding, Pengshan Xie, Jingwen Wang. ✉e-mail: jiasun@csu.edu.cn; johnnyho@cityu.edu.hk

interface, where no electrochemical reaction occurs, these sensors can achieve stable, non-destructive sensing[10–12]. NFJ acts like a capacitor coupling ionic/electronic currents with a charge-voltage curve sensitive to mechanical signals[13]. These sensors are self-powered, with output depending on anion/cation concentration differences between the NFJ and the hydrogel center[10,14]. However, similar mobility of anions and cations limits ion separation and results in a thin ion atmosphere (i.e., Debye length), leading to insufficient self-generated voltage[15]. MXenes, a family of 2D transition metal carbides/nitrides, offer abundant hydroxyl groups and superior in-plane carrier mobility, forming crosslinked conductive networks with hydrophilic polymers like PVA[16,17]. Protons can be easily ionized from the nanosheets and transported through selective ion microchannels to generate electrical energy[18,19]. However, in vertical piezoionic mechanoreceptors, pressure is dissipated by horizontal deformation, affecting sensing performance. On the other hand, with its lower Young's modulus, PVA hydrogel enhances interfacial adhesiveness and reduces dissipation through microstructure engineering, but fabricating homogenous hydrogel microarrays remains challenging[20–22].

In this study, we constructed an NFJ by connecting ionic-conducting hydrogel microneedles (HM) with electronic-conducting ITO, addressing non-flexibility and transmission-loss issues in piezoelectric ceramics. Finite element analyses (FEAs) optimized the structural parameters of the stress-concentrated ion-transport layer. We explored the piezoionic mechanism in 2D materials, finding significant interlayer spacing changes in MXene nanosheets under stress facilitated by a biomimetic microstructure. This allowed unidirectional proton transport through microchannels, amplifying the proton gradient and enhancing piezoionic efficiency. Consequently, the mechanical sensing unit (HM-S) achieved high power density and sensing stability. Integrated with a neuromorphic computing unit, the artificial piezoionic mechanoreceptor enabled multimodal object identification, distinguishing texture, shape, and category. Using an artificial neural network (ANN) and deep learning, our e-skin system achieved up to 90% accuracy in recognizing objects like metal, rubber, fabric, foam, and plastic. This biomimetic design offers new insights into enhancing sensitivity and stability for self-powered mechanoreceptors.

Results

Biomimetic microstructure design of stress-concentrated HM

As the main nerve ending beneath the skin, the Merkel cell (texture recognition organ) plays a vital role in the light-touch response, owing to the clamshell-like dendritic structure (Fig. 1a)[23]. While tactile nerve endings receive mechanical stimuli, protein channels will allow cations to flow into postsynaptic neurons[24]. Inspired by the structure and sensing mechanism in biological skin, the piezoionic sensing unit was rationally assembled by polydimethylsiloxane (PDMS), stress-concentrated HM, and PET/ITO electrode (Fig. 1b). Here, HMs were fabricated through sol-gel transition and vacuum-refill process to conquer the dispersion and structural inhomogeneities (Supplementary Fig. S1). The biomimetic microstructure design contains two subparts: (i) HM serves as a stress-concentrated layer to enhance sensitivity and conversion efficiency; (ii) Directionally aligned MXene nanosheets act as a selective ion-microchannel to amplify the proton gradient. The interlayer spacing of nanosheets will narrow the stress-concentrated area while stress is applied to HM-S, resulting in tip-to-base proton diffusion alongside each conic. With the stress released, protons undergo reverse diffusion under osmotic pressure due to the high proton concentration in the basal region, where the interlayer spacing is relatively wide. Accordingly, the active and passive proton migrations constitute a neuron-like transmembrane action potential. Figure 1c illustrates HM's vertical/horizontal strain distributions and homogenous microstructure, indicating the stress concentration at the conical tip and consistent mechanical-electrical response at each

conic. In-situ characterizations were conducted to elaborate on the effect of stress-induced interlayer spacing on proton transport efficiency (Supplementary Figs. S2, S3). As a result, the stress-concentrated structure was conducive to increasing the interlayer spacing variation, enlarging the ion gradient between the stress-concentrated region and the hydrogel-electrode interface. Combining ANN and deep learning, our in-sensing and computing e-skin system achieved effective sensing and discrimination of different types of objects (Fig. 1d).

The most common design among the self-powered sensors involves bonding a silicone rubber layer with microstructures to a rigid metal electrode[25,26]. During pressure loading, the sensor detects the external stimuli mainly through the elastic deformation of microstructures. Its sensitivity ($S_O O$) can be derived by force-electric coupling modeling and can be expressed as[27]

$$S_0 = \frac{3q_0 kh}{E\varepsilon_0} \tag{1}$$

where E denotes Young's modulus of the micro-structured PDMS layer, h is the gap distance of the initial status, k is the mechanical transfer efficiency, and q_O and ε_O represent the charge density and vacuum permittivity (constants), respectively. In Eq. 1, Young's modulus, height of the PDMS layer, and mechanical transfer are the critical factors in improving sensitivity. However, the materials with low Young's modulus would lead to inefficient mechanical transfer due to their residual strain and transverse stretching. Thus, achieving high sensitivity of the self-powered mechanoreceptor through structural modulation is still challenging.

In our design, HM replaced the conventional PDMS layer to attach to PET/ITO films to decouple the competing effect between Young's modulus and mechanical transfer. Specifically, PVA-based hydrogels possess modulable E and adhesiveness to ITO substrates, which can reduce the gel-electrode interfacial gap to enhance stability and mechanical transfer efficiency[28]. The oriented MXene nanosheets will also utilize the residual strain and transverse stretching of PVA chains, directing carriers to be transported to the ITO electrode. Characterizing morphology, elements, and interlayer spacing illustrated the successful synthesis of few-layered MXene nanosheets (Supplementary Figs. S4, S5). More significantly, the aspect ratio (H/D) of cones will influence mechanical-electrical conversion as the electric field distribution in the HM layer is related to the angle of the inclined plane of the cones with respect to the horizontal plane, leading to a non-monotonic relationship between the aspect ratio and S_O[29]. To investigate the effect of conical geometry on mechanical response, FEAs were conducted by utilizing COMSOL software. Under the same stimulation (2778 Pa), the displacement of HM was more significant than that of the bulk structure, demonstrating the stress concentration in microneedle tips and high sensitivity of HM-S (Fig. 2a).

Besides, we fabricated HMs with different aspect ratios. Still, the same microneedle intervals were used, and corresponding structural simulations (piezoresistive mode) were performed (as illustrated in Fig. 2b) (specific parameters were shown in Supplementary Table 1). Homogeneity of HMs (C1-C5) could be observed from SEM images, indicating the engineering universality of this material combination, and significant distinctions of sensing potential between C1-C5 were displayed in the inserted FEA figures (top view of the cones). Retrieving the overall resistance and surficial strain, respectively, under different stimulations (0-2778 Pa), stress-resistance, stress-strain, and gauge factor (GF)-aspect ratio plots can be derived. The stress-concentrated microneedle structures possessed higher sensitivity and GF than the bulk structure and achieved the maximum value of GF (4.05) when the aspect ratio equals 1.76 (Supplementary Fig. S6).

Considering the ion transport mechanism in HM, calculations were further carried out in capacitive mode, and apparent distinction of capacitance changes between HM and bulk hydrogel can still be

observed (Fig. 2c). When aspect ratio is increased from 0.67 to 2.31, the capacitance variation under pressure of 2778 Pa is raised from 7.38 % to 13.42 %, indicating the trends in sensitivity is dominated by the gap distance (h) in this case. However, while further increasing the aspect ratio to 2.67, the corresponding sensing value decreases to 11.54 %, suggesting 2.31 is the optimal solution for the aspect ratio in capacitive mode. To intuitively illustrate the specificities of our biomimetic microstructures, the electric field distribution and surface energy density of sensing units (HM and bulk) were shown in Fig. 2d, e, respectively. The direction of the normal to electric field contours tends to be horizontal at the edges in bulk structure, while the contours spread vertically in the direction of the conic height in HM, indicating the efficient mechanical-electrical energy conversion of microneedle structures. Moreover, the energy density at the surface of

the HM layer is more concentrated in needle-tip areas and possesses a higher peak value (3.2 mPa) than that of the bulk layer (1.5 mPa). Combining the FEAs in piezoresistive, capacitive, and piezoelectric modes, the aspect ratio is within the range of 1.76-2.31 to achieve optimal sensitivity. To obtain sensitivity in case of self-powered sensing, open-circuit voltage (V_{oc}) under different stresses was measured (contacting object: polyethylene (PE) film) (Supplementary Fig. S7). The sensitivity of HM-S with different aspect ratios (0-2.66) equals the corresponding slope of V_{oc}-stress curves, so we performed a linear fit to the raw data. As a result, the sensitivities of HM-S with bulk structure, C1, C2, C3, C4, and C5 parameters were 226 mV kPa^{-1}, 2096 mV kPa^{-1}, 2452 mV kPa^{-1}, 1766 mV kPa^{-1}, 1556 mV kPa^{-1}, and 839 mV kPa^{-1}, respectively. Compared with simulation results, the maximum sensitivity value was obtained at C2 instead of C1, and the
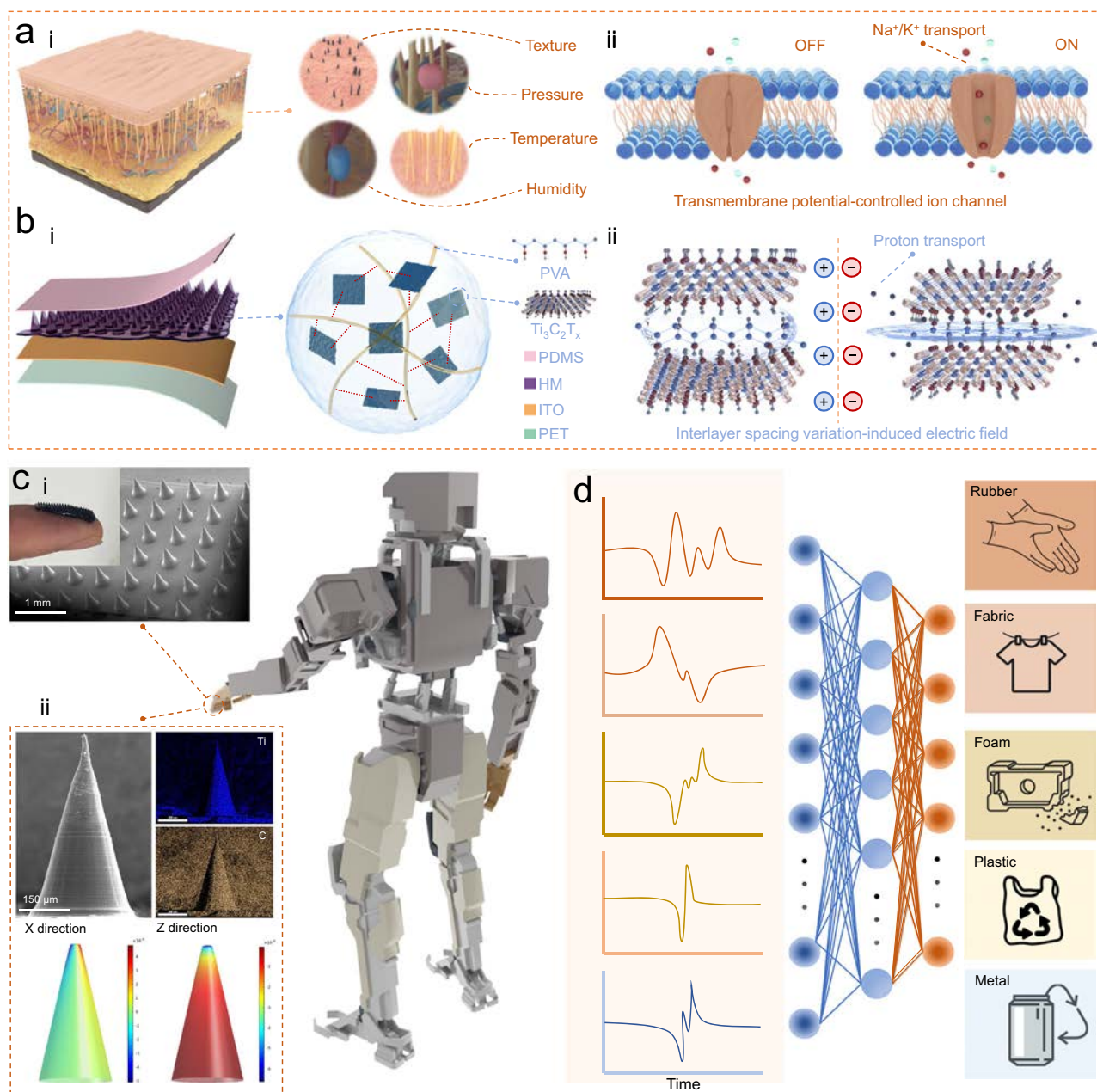

Fig. 1 | Object recognition system inspired by human skin. a Schematic diagram of skin organs and ion channels on cell membranes. **b** The structure of HM-S (**i**): Polyvinyl alcohol/Ti$_3$C$_2$T$_x$ (PVA/MXene) composite hydrogel microneedle (HM) was adhered on the polyethylene terephthalate/indium tin oxide (PET/ITO) substrate, followed by polydimethylsiloxane (PDMS) encapsulation. The conductance mechanism of HM-S (**ii**): Proton transport induced by interlayer spacing variation of MXene nanosheets. **c** Morphologies (**i**), elemental characterization, and FEA of HM (**ii**), with the application concept of human-machine interaction. **d** Multimodal object identification with an artificial neuromorphic network (ANN).
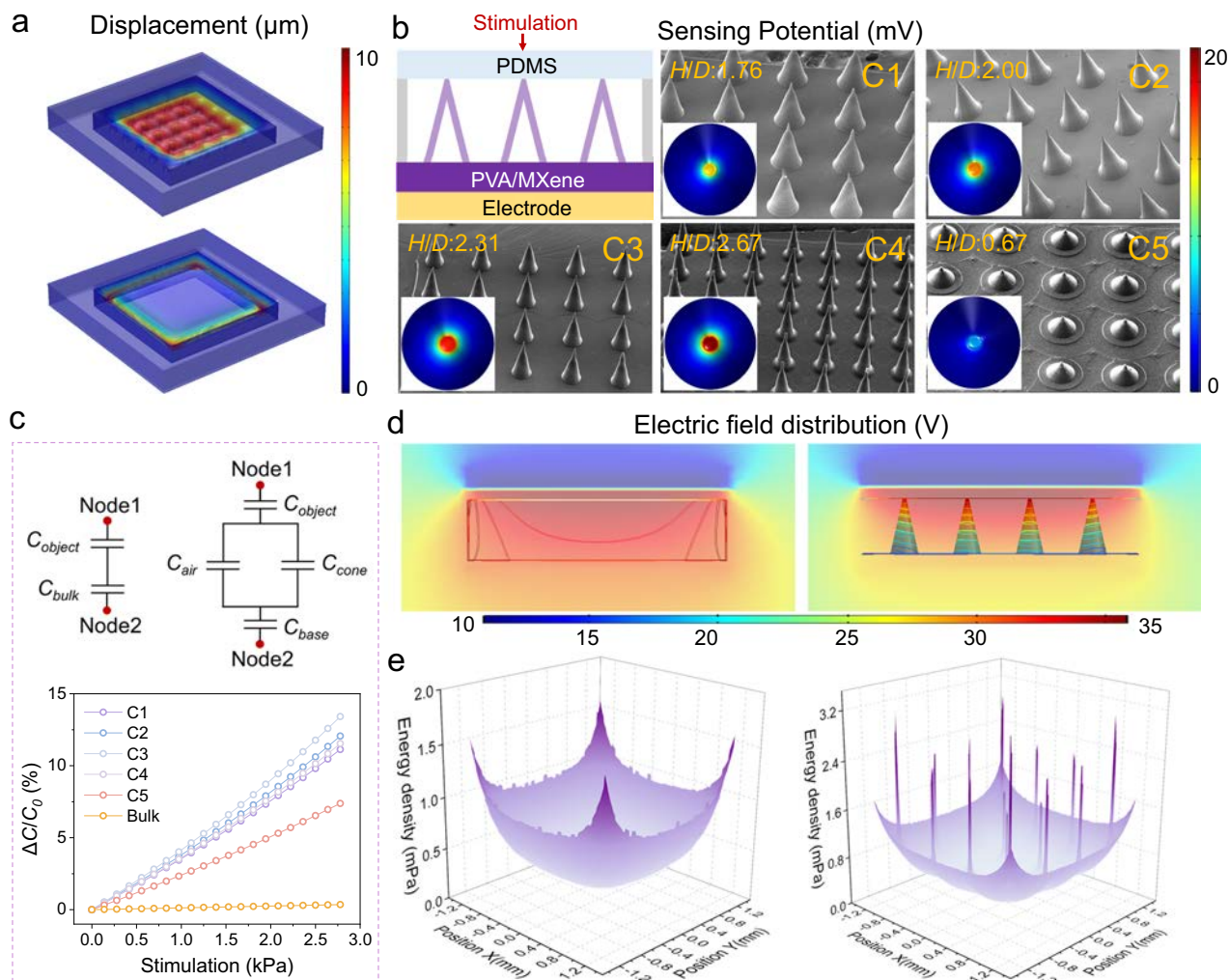
Fig. 2 | Finite element analyses (FEAs) investigating the effect of geometric properties on mechanical response. a A 3D plot comparing the displacement of HM-S and bulk hydrogel mechanoreceptor under a fixed load. **b** Schematic demonstration of the device's modeling structure, surface morphology, and contact potential. (*H* and *D* represent the height and caliber of the cone, respectively. PDMS: Polydimethylsiloxane; PVA/MXene: Polyvinyl alcohol/Ti$_3$C$_2$T$_x$). **c** Schematic of the modeled circuit and comparison of capacitance changes ($\Delta C/C_O$) between microneedle and bulk structures versus external stimuli. (C_{object}, C_{bulk}, C_{air}, C_{cone}, and C_{base} represent the capacitances of the contacting object, bulk structure device, air, cone part of the HM, and base part of the HM). **d** Comparisons of electric field distribution, and **e** energy density between the bulk mechanoreceptor and HM-S.

structural parameters of C2 are eventually chosen to fabricate the multimodal sensing unit (HM-S).

Piezoionic effect in proton transport-dominant HM

In biological systems, the ion channels controlled by intracellular Piezo proteins enable tactile perception[30]. Similarly, our system exists with proton transport-dominated piezoionic effect (Fig. 3a): (i) As specific stress is applied on HM-S, the stress-concentrated area will generate larger deformation, decreasing the interlayer spacing of MXene nanosheets, while less variable morphology will be present in the gel layer near the base (Supplementary Table 2); (ii) Afterwards, protons are ionized from -OH groups on the nanosheets or H$_2$O molecules, and transport unidirectionally from areas with narrow spacing to the wider ones. In the hydrogel state, protons can be transported through a hydrogen bonding network constructed between H$_2$O molecules (Grotthuss mechanism)[31] or alongside the continuous hydrogen bonding wires formed between PVA and MXene (interlayer transport)[32] or hopping between PVA chains induced by the mechanical-loss-generated internal energy (thermally-activated proton hopping)[33]. The ionic conductivity (σ) is related to water content, temperature, and ionization process, which

can be expressed by the following equations[31,34]

$$\sigma = k_p w^d \tag{2}$$

$$\sigma = \sigma_0 T^{-\frac{1}{2}} e^{\frac{-E_a}{k_B(T-T_0)}} (T > T_g) \tag{3}$$

$$E_a = -k_B T \ln K \tag{4}$$

where w is the water content in hydrogel, k_p and d represent the proportionality factor and critical exponent, and σ_O denotes a pre-exponential factor. T and T_O are the given temperature and a reference Vogel temperature (equal to glass transition temperature: T_g in ideal conditions), respectively. E_a and k_B represent the activation energy and Boltzmann constant, respectively, and K is the ion product constant. To improve piezoionic efficiency, enlarging the ion gradient at the electrolyte/electrode interface is a common approach that presupposes rapid cation/anion separation[35]. Accordingly, a continuous and dynamic hydrogen-bond crosslinked network was constructed in PVA hydrogels by introducing 2D MXene nanosheets. Compared with
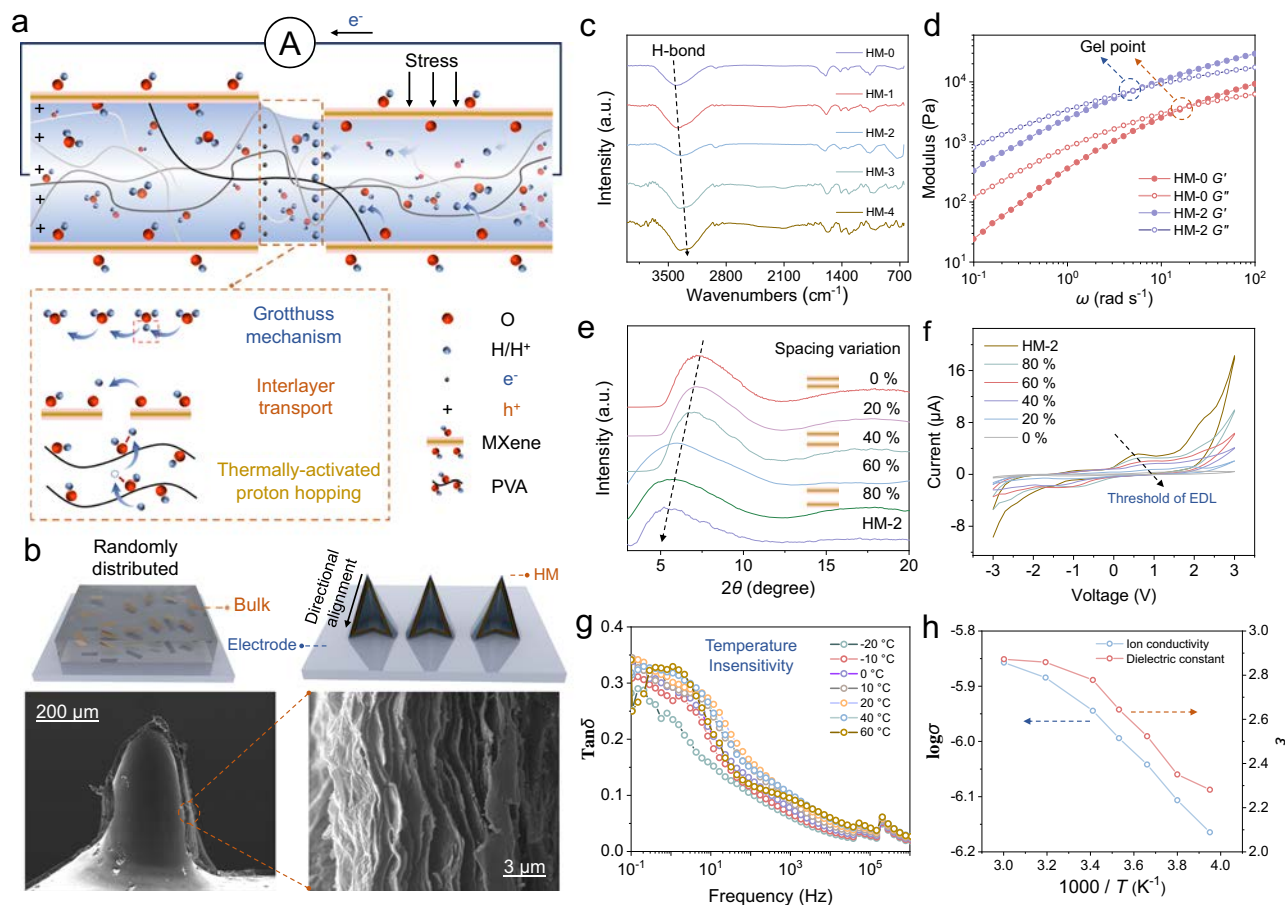
Fig. 3 | Piezoionic effect generated by interlayer spacing variation-induced proton transport. a Schematic illustration of the piezoionic effect in HM with proton-dominant transport. **b** Structure comparison between the bulk hydrogel and HM, with the cross-section morphology of HM. **c** FT-IR spectroscopy of HM with different MXene contents. **d** Rheological behavior of HM displaying the gel-point variation. **e** XRD, and **f** *I-V* curves of HM-2 with different water contents, indicating that the interlayer spacing variation induced the proton transport. The channel length (100 μm) was controlled. **g** Wideband dielectric testing of PDMS-encapsulated HM-2 under the temperature range of -20 to 60 °C (δ is the dielectric loss angle). **h** Conductivity (σ) and permittivity (ε) variation of the hydrogel versus temperature.

the bulk structure formed by mechanical mixing (the randomly distributed porous structure was displayed in Supplementary Fig. S8), PVA/MXene composites were reoriented, which was driven by air pressure under the microneedle fabrication process (Fig. 3b). Combining the stress-concentrated microstructures, protons transduce unidirectionally and rapidly through the microchannels. At the same time, the mobility of negatively charged MXene nanosheets is limited by spatial site resistance effects, resulting in ion gradient enlargement and efficient energy conversion.

MXene nanosheet is the primary proton transport medium, a superior electronic conductor, and an additive for mechanical enhancement. Hence, the hydrogel content is a critical index affecting the piezoionic efficiency of HM-S. With the increasing content of nanosheet, the vibrational peak of -OH groups shifted to lower wave numbers, indicating the stronger hydrogen bonding between PVA and MXene (Fig. 3c). Additionally, the coordination of hydrogen bonding weakens the binding of oxygen atoms to hydrogen atoms on the -OH groups, contributing to easier ionization of protons from the MXene surface (increased K), thus resulting in enhanced ionic conductivity according to Eq. 3 and Eq. 4. However, owing to the agglomeration of nanosheets, the ionic and electrical conductivity of HM decreased when the content reached to 6% and 8%, respectively (Supplementary Fig. S9). Furthermore, under the same temperature and strain, rheological behaviors of HM with different MXene contents were compared, as displayed in Supplementary Fig. S10. The storage/loss

modulus (G'/G'') was enhanced at low angular frequencies as the nanosheet content rose from 0 to 4 %. At the same time, G' of the hydrogel declined approximately an order of magnitude (from 10^3 to 10^2) when MXene content further increased. To satisfy the requirements of tactile perception, the homogeneity of the HM structure and sensor stability are significant. Consequently, 4 % MXene content (HM-2) was selected as the optimal proportion, and the gel point shifted to lower frequencies compared with that of HM-0, indicating the improved reconfigurability and processability of HM-2, which possessed the generalization of microstructure engineering (Fig. 3d).

The minimized interlayer spacing and increase in voltage threshold of the electronic double layer (EDL) with the gradual dehydration of HM-2 indicated that the narrowing of interlayer spacing decreased proton mobility (Eq. 2 and Supplementary Fig. S11), further facilitating the proton/MXene separation and proton gradient enlargement under stress (Fig. 3e, f). In hydrogel state, HM-2 possessed lower voltage threshold (0.6 V) and higher peak current (3.14 μA), compared with that of PVA/H_2SO_4 system (0.8 V and 0.05 μA, respectively) when H_2SO_4 content in the hydrogel was controlled to be 4%, indicating the presence of interlayer transport in MXene-based hydrogel, an advantage over ionic hydrogels in terms of piezoionic efficiency (Supplementary Fig. S12). Notably, the water content of the hydrogel was controlled by natural dehydration and PDMS encapsulation. If the fresh hydrogel were encapsulated in its initial state, the humidity (from 0 to 95%) would hardly affect the water content and conductivity of the

hydrogel under ambient temperature (25 °C) (Supplementary Fig. S13). Ambient temperature variations will also modulate ion mobility and segmental flexibility, affecting the sensing performance according to Eq. 3. At low frequencies (Fig. 3g), loss angle tangents of HM-2 under different temperatures were all below 1 (0.25-0.35) and initial capacitances were at the lower order of magnitude (10 pF, Supplementary Fig. S14), indicating the lower ion diffusion relaxation and efficient energy conversion. Besides, HM-2 exhibited temperature insensitivity while being conducted dielectric testing under -20 to 60 °C, avoiding interference of temperature changes on tactile perception (Fig. 3g). Retrieving values at the same frequency (100 Hz), there was a relationship between the magnitude of conductivity and inverse of temperature that the inclination (absolute value) decreased with the increasing temperature, implying the inhibitory of rational assembly to thermally-activated proton hopping (Fig. 3h). Additionally, the variation of permittivity with temperature was negligible, further confirming superior environmental stability of HM-S (Fig. 3h).

Output/sensing performance and application demonstration of HM-S

In a typical nanogenerator system, large transmission loss will be caused by interfacial gaps/voids due to the mechanical mismatch between the transport layer and electrode[36,37]. As for MXene-based hydrogel, dehydration and oxidation will occur, affecting the structural stability and generating piezoelectric power (the interaction between TiO_2 and nanosheets), which may influence output performance. To enhance interfacial adhesiveness and construct NFJ between HM and ITO, PVA/MXene gel solution with the same content (4% MXene) was coated on the PET/ITO film first, then hitch HM-2 to the coating. The hydrophilic coating endowed an interfacial mechanical match between HM and ITO, leading to higher interfacial peel strength and cyclic-test stability of the device (Supplementary Fig. S15). By oxidation mechanism analysis of PVA/MXene hydrogel, PDMS encapsulation was conducive to slowing down the dehydration and oxidation when the hydrogel was exposed to air. At the same time, the corrosion-prone electrode could promote the formation of TiO_2 (Supplementary Figs. S16-S18, detailed description was shown in Supplementary information). Herein, we replaced the conventional Cu electrode with PET/ITO, and the electrochemical window of the hydrogel-ITO interface was wider than that of the hydrogel-Cu foil, indicating NFJ was constructed in HM-S, eliminating the oxidation effect of the electrode (Supplementary Fig. S19). Through a modularization strategy, HM-S with larger sizes (3 cm^2, 5 cm^2, 10 cm^2) could be spliced by the HM unit (1 cm^2) to conquer the limitations of molding flexibility and allow them to be freely assembled according to the human or robotic contours (Supplementary Fig. S20). The corresponding piezoionic performances were shown in Fig. 4a, b. The open-circuit voltage (V_{oc}) and short-circuit current (I_{sc}) of the HM-S unit (1 cm^2) were 5.1 V and 11.6 nA, and achieved 71.5 V and 180.1 nA with the size of 10 cm^2, respectively, indicating almost linear superposition of total piezoionic power by stacking the sensing units. Besides, the V_{oc} reached 9.3 V in slight-contact mode, implying these mechanoreceptors demonstrated superior sensitivity (Fig. 4c). Additionally, by increasing the thickness of polyimide (PI) film support behind the mechanoreceptor (from 10 to 50 μm), the short-circuit currents of HM-S under incremental deformation (from 1 to 5%) were 11.4 nA, 61.2 nA, 245.2 nA, 425.3 nA, 565.1 nA, respectively, reflecting slight strain perception of the mechanoreceptor (Fig. 4d and Supplementary Fig. S21). Since the mechanical-electrical response of HM-S was hardly impacted while changing the contact frequencies (Fig. 4e), the normalized test conditions for object identification were selected as 1.5 Hz and 2% strain. To compare the output performances of HM-S and the sensor with a bulk hydrogel layer, a resistance box ($10^4 Ω$-$10^9 Ω$) was loaded on the piezoionic mechanoreceptors, and the power density (output power/sensor size) was calculated. As a result, HM-S possessed a higher power density (165.6 mW m^{-2}) than that of the bulk structure (28.9 mW m^{-2}), confirming the superior sensitivity and mechanical-electrical conversion efficiency of HM-S with stress-concentrated biomimetic microstructure (Fig. 4f).

Depending on the hardness/roughness/insulation differences between materials, distinct total powers could be produced when HM-S was touched by various contact objects (Fig. 4g and Supplementary Fig. S22). Due to the high sensitivity of HM-S (microneedle), there was a larger discrimination of material characterization voltages/currents compared with the bulk structure. For instance, when contacting carbon fabrics (object 1), open-circuit voltages of HM-S and bulk hydrogel sensor were 29.1 V and 6.9 V, respectively; while touching Al foils (object 10), the voltages were 1.8 V and 0.2 V, respectively. Moreover, benefiting from the homogenous stress-concentrated microneedle arrays, texture recognition of cotton fabrics could be achieved by combining signals of press and shear modes (Fig. 4h). As for piezoionic mechanoreceptor, the sensing mechanism can be divided into four steps[38]: (i) While stress (press/shear) is applied on HM-S, vertical/horizontal deformations of HM will present and proton concentration gradient alongside direction of displacement begin to be generated; (ii) When stress is reached its maximum, protons continue to transport until ions/electrons at the surface/electrode attain equilibrium, forming non-faradaic junction; (iii) As stress is released, the elastic deformation will recover and lead to a reverse proton transportation; (iv) HM-S is reset after emerging two pulses (positive/negative). With the increasing ampacity (A) of fabric, the short-circuit currents of HM-S were all diminished in two modes due to the reduced point-point contact frequency between the microneedle tip and fiber nodes (Fig. 4i and Supplementary Fig. S23). Notably, the shear force between HM-S and fabrics was continuous and decreased with contact area, leading to differences in waveforms and outputs.

To demonstrate the application potential of wearable integrated devices and inter-finger synergistic while grabbing objects with different shapes, five HM-S mechanoreceptors were bonded on the fingers, and one light emitting diode (LED) bulb was on each mechanoreceptor (Fig. 4j). It should be noted that ITO ($10^2 Ω cm^{-2}$) electrode was replaced with a copper foil ($10^1 Ω cm^{-2}$) to ensure excellent electrode contact during gripping. While touching rugby with the ellipsoidal shape, indicators representing the thumb (a), middle (c), and ring (d) fingers flashed with different frequencies, yet there was no apparent response in terms of the index (b) and little (e) fingers (Supplementary Movie 1). Besides, two-finger coordination (e.g., thumb/middle and index/little) could be observed as grabbing a basketball (Supplementary Movie 2). It is noted that different shapes of grasps lead to differences in finger force generation. Furthermore, all fingers were required to be firing when the object was relatively large and uniformly stressed (football) (Supplementary Movie 3). In the cyclic test, HM-S can achieve a stable output for up to 10,000 cycles, indicating that NFJ contributed to sensing stability (Supplementary Fig. S19). Besides, after natural aging and harsh environmental aging tests, the shape and mass of the device barely changed compared with the initial state, and the output performance of HM-S was maintained in a certain range (50-100 nA) (Supplementary Fig. S24). Compared with conventional self-powered mechanoreceptors, our device possessed higher sensitivity and power density due to the structure optimization (Supplementary Fig. S25 and Supplementary Table 3). These results confirmed the superior sensitivity, self-powered capability, and practical longevity of HM-S, which can effectively distinguish the main fingers used when grasping different objects. The prototype was conducive to realizing accurate object recognition and energy saving of wearable electronics. By analyzing and implementing human gripping habits in algorithms, the artificial tactile system (e.g., robot arm) is expected to recognize objects via the multimodal perception of different micro/macro morphologies (textures/shapes).
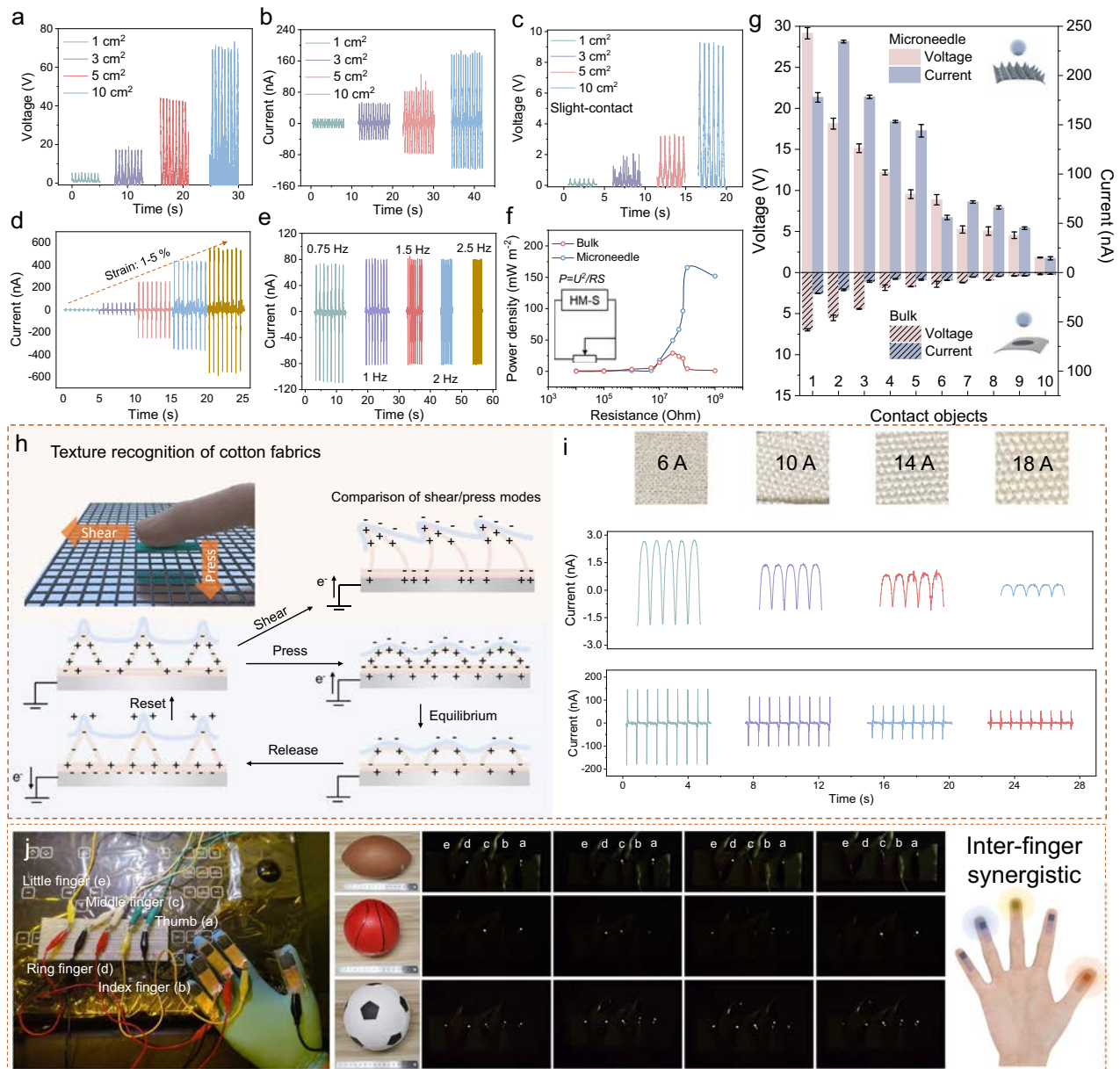
Fig. 4 | Output/sensing performance and application demonstration of HM-S.
a V_{oc}, and **b** I_{sc} of HM-S with different sensing unit sizes. **c** V_{oc} of HM under slight-contact mode (0 % strain). **d** I_{sc} of HM-S under different strains and, **e** various frequencies. **f** The relationship between calculated power density (P) and resistance (R) of external loads (U and S represent the generated voltage loaded on resistance box and device area, respectively). The contact pairs were fixed as PE/HM-S for (**a**)-(**e**) and carbon fabric/HM-S for (**f**). **g** V_{oc} of HM-S and bulk hydrogel mechanoreceptor with distinct contact objects. The error bar illustrated in each column was obtained by calculating the mean and variance of the five peaks. **h** Texture recognition of cotton fabrics achieved by HM-S with shear/press modes (A is the fabric ampacity, reflecting the roughness of fabrics). **i** I_{sc} of HM-S while touching cotton fabrics, different am in shear (up) and press (down) modes. **j** Shape identification of polyvinyl chloride (PVC) balls by detecting the brightness and flicker frequency of the LED.

Neuromorphic computing-enabled object identification

Tactile sensation is the earliest and most fundamental sense owned by the human body, and it is also the most widespread, complex, and unique sensory system. Touch converts pressure from various materials into electrical signals through tactile corpuscles embedded in the skin. The brain interprets and processes these signals, facilitating experiential learning and knowledge accumulation over time[39]. For deep learning neural networks, parallel matrix operations and low power consumption are important for matching algorithms at the physical level. The core computation of neural networks is Matrix-Vector Multiplication (MVM), where the synaptic weights of the neural network and the input signals of the neural network perform matrix operations. Memristors with predominantly row and column structures fulfill the need for parallelism, low power consumption, and matrix operations[40]. Inspired by this structure and process, we combined a multimodal sensing unit and arithmetic unit to fabricate the e-skin composed of electronic tactile corpuscles designed to convert tactile signals from the biological world into electrical signals readable by electronic systems (Fig. 5a). The structure of the single arithmetic unit is ITO/Al_2O_3/Pt/Ag, which is classic Ag-based diffusive memristors[41]. Formation and fracture of silver metal filament in the 10nm Al_2O_3 thin layer when scanned with positive and negative voltages applied to the active electrode Ag (Fig. 5b). In the cycling test, the device can complete the switch between high resistance state (HRS) to
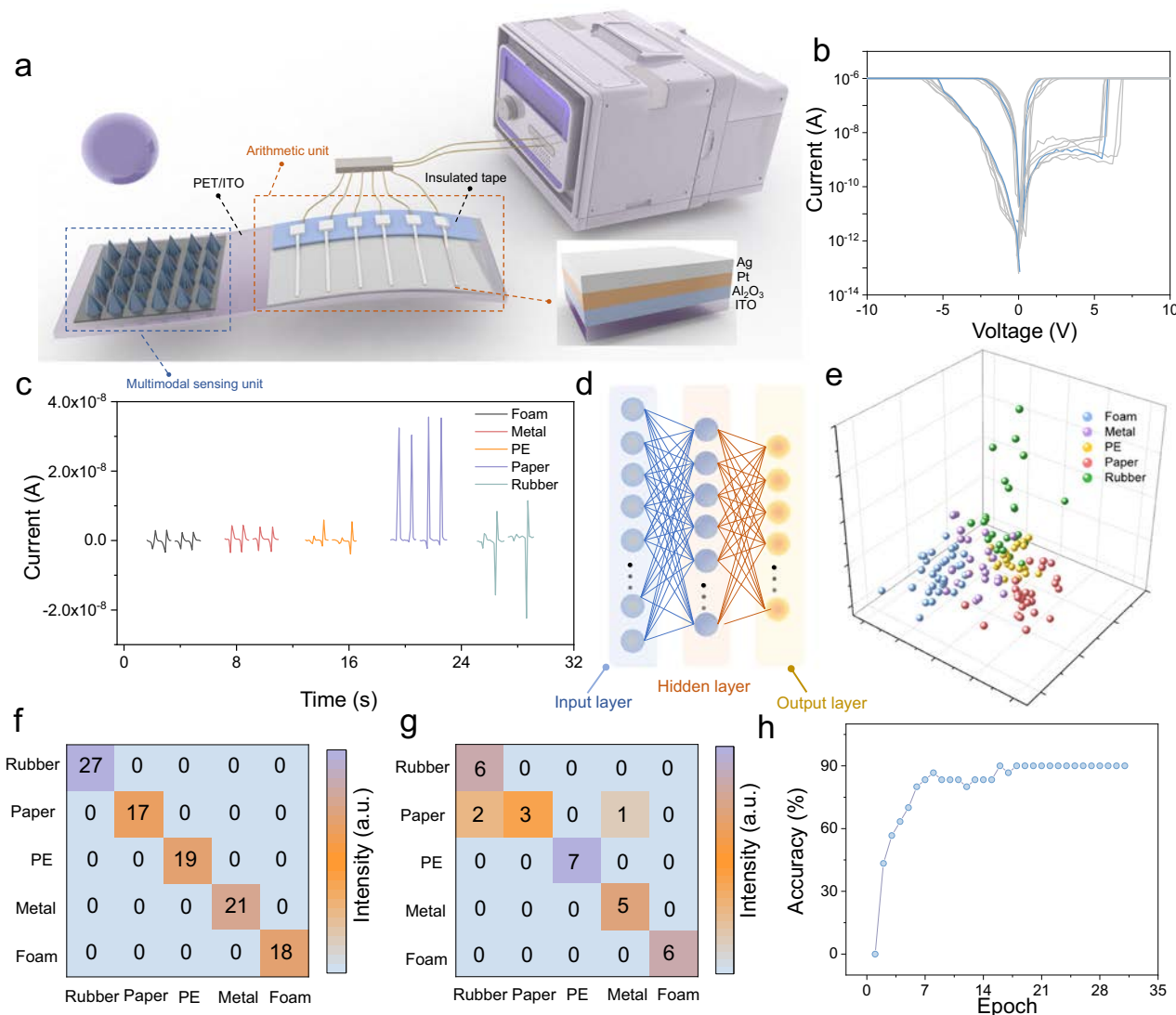
Fig. 5 | The fabrication and algorithm-hardware combination of in-sensing and computing e-skin. a Composition of sensing computing arrays, including HM-S and Ag-based memristor arrays. **b** Typical *I-V* characteristics of the ITO/Al$_2$O$_3$/Pt/Ag device in multiple tests under 10^{-6} A compliance current (*I$_{CC}$*). **c** Current signals generated by a memristor array during regular contact with different sensing array materials. **d** Schematic of a three-layer artificial neural network. **e** The distribution of the high-dimensional feature vectors generated by the e-skin using the LDA method. The independent confusion matrices for (**f**) the training and (**g**) test sets. **h** The recognition accuracy of the in-sensing and computing e-skin.

low resistance state (LRS) under 1000 cycles, indicating the good robustness (Supplementary Fig. S26). Compared with the only Ag active electrode (Supplementary Fig. S27), adding 2 nm of Pt inert metal can effectively reduce the migration rate of Ag and Ag$^+$ during redox reactions and improve the overall thermal stability of the device[42,43]. Integrating a self-powered sensing unit with a neuro-morphic computing unit (memristor) is similar to supplying the LED bulbs with the mechanoreceptors. The voltage loaded on the LED (*V$_{out}$*) must reach the rated voltage to light it (1.5 V), and the value of *V$_{out}$/V$_{oc}$* corresponds to the ratio of load impedance to total circuit impedance (*R$_{load}$/R$_{total}$*) (Supplementary Fig. S28). As for the memristor, the impedance difference is enormous between LRS and HRS, resulting in output variation under state switching. Additionally, the fire/reset of the memristor is related to the amplitude/direction of *V$_{out}$*. When the forward self-generated signals fire the memristor, the state of the memristor will transfer from HRS to LRS, and the reverse signals will reset the memristor from LRS to HRS. Besides, there may not be a state transition if the amplitude is low. Owing to the differentiation of *V$_{in}$*

(*V$_{oc}$*) while HM-S contacts various objects, the fire/reset behavior will be different, which leads to the corresponding characteristic signals.

To demonstrate the effectiveness of this e-skin, we selected five materials: foam, metal, polyethylene (PE), paper, and rubber, repre-senting both environmentally friendly and non-friendly categories. Specifically, in the case of the same integrated unit, the perceptual unit was stimulated with the same test conditions. The voltage was gener-ated at the sensing unit and applied to the back-end memristor arrays through the bottom electrode to realize the conversion of the pressure signal to a computable electrical signal. Consistent with the previous results, due to the ultra-sensitivity of the multimodal sensing unit to different materials, different material-induced voltage signals would produce corresponding characteristic current peaks (Fig. 5c). To fur-ther illustrate the uniqueness of these responses and validate that the e-skin can indeed convert tactile sensations into electronic signals interpretable by the digital world, we employed a three-layer artificial neural network with a configuration of 20-10-5 to classify the respon-ses of the five materials (Fig. 5d)[44,45]. All response features are

pre-resized to a uniform dimension of 20×1 to retain the primary information. Furthermore, as shown in Fig. 5e, we visually represented the distribution of the high-dimensional feature vectors generated by the e-skin by reducing the data to three dimensions using the Linear Discriminant Analysis (LDA) method, where color denotes the material type[46]. Samples of the same category cluster closely, while different categories are more distinct. Figure 5f, g presents the independent confusion matrices for both the training and test sets, with strong diagonal dominance indicating high classification accuracy across tasks. The accuracy epochs on the test dataset are illustrated in Fig. 5h throughout the training process, peaking at 90%[47]. The in-sensing and computing e-skin, integrated by two sensing and computing units, demonstrates effective sensing and discrimination of different objects and materials.

Discussion

Inspired by biological skin, we successfully constructed stress-concentrated and homogenous microarrays and oriented ion-microchannels in a dynamic crosslinked PVA/MXene composite system to improve the sensitivity of piezoionic mechanoreceptors. Our biomimetic design included twofold: (i) Microarrays served as tactile organs perceiving faint stresses; (ii) Nanosheets acted as selective ion-microchannels to amplify proton gradient. The dynamic hydrogen bonds formed between PVA and MXene facilitated proton/MXene separation and provided a continuous proton transmission environment. Furthermore, the significant interlayer spacing variation of MXene nanosheets induced ion gradient enlargement by tip-to-base proton transport. Through structural optimization, the hydrogel's mechanical transfer efficiency and sensitivity were further enhanced, and the assembled sensing unit (HM-S) possessed a higher power density ($165.6\,\mathrm{mW\,m^{-2}}$) than that of the bulk structure. Due to our sensing unit's high sensitivity, texture/shape/category multimodal recognitions were achieved by contacting different objects in a normalized condition, and our tactile perception system with an ANN algorithm support exhibited superior accuracy (90 %). Moreover, due to non-destructive ionic/electronic coupling (NFJ) at the hydrogel/electrode interface and the homogenous structure of the microarrays, our e-skin system demonstrated exceptional stability through rational assembly, ensuring stable sensing and switching for over 10,000 cycles. This biomimetic design, combining ion-microchannel construction and microstructure engineering, paved a path to decouple the competition between sensitivity and stability of artificial mechanoreceptor/e-skin, enhancing recognition accuracy for practical application.

Methods

Measurement and characterization

The piezoionic sensing performances were evaluated by a periodic impacting test with a linear motor (HS01-37 166, NTI AG, USA) as the impact source. The V_{oc} and I_{sc} were collected on a Keithley 6514 system electrometer and an SR570 low-noise current amplifier, respectively. The device's deformation and impact frequency were controlled by controlling the thickness of the PI film support behind the mechanoreceptor and the speed of the motor, respectively. Finite Element Analyses (FEAs) were conducted using COMSOL Multiphysics software (ver 5.4, COMSOL Inc., USA). The solid and electrostatic modulus was used to analyze the strain-stress and corresponding resistance/capacitance/electrical field distributions under different geometrical structures. The main steps below are Design Geometry-Define Materials-Set Boundary Conditions and Loads-Set current terminal/ground-Meshing-Study and Solution. Fourier transform infrared (FTIR) spectra were collected on a Nicolet 6700 spectrophotometer (Thermo Scientific, USA) in Attenuated Total Refraction (ATR) mode from 400 to $4000\,\mathrm{cm^{-1}}$. The rheological behaviors of the hydrogels were tested by an ARX2000EX rheometer (TA Instruments, USA). The hydrogel samples were molded into 25 mm discs, and the test procedure was performed with 1% strain applied, with a shear rate range of 100-0.01 Hz and a test temperature of 25°. Transmission electron microscopy (TEM) images were obtained using FEI Tecnai G2 F20. Elemental maps were taken by FEI Nova NanoSEM 450. X-ray diffraction (XRD) tests were conducted on a PANalytical Empyrean diffractometer with a scanning range from 3° to 70°. X-ray photoelectron spectroscopy (XPS) spectra were obtained using a Kratos XSAM800 spectrometer. The morphologies and EDS mapping of as-prepared PVA/MXene composite microneedles were examined using scanning electron microscopy (SEM, Quanta 450 FEG, FEI). The variable temperature dielectric testing in the frequency range of 10^{-1}-10^{6} Hz was obtained by using a broadband dielectric impedance relaxation spectrometer (Concept50, Novocontrol GmbH, Germany), and the thickness and diameter of the circular encapsulated hydrogel specimen were 2 mm and 20 mm, respectively.

Synthesis of exfoliated $Ti_3C_2T_x$

First, 2 g LiF was dissolved in 40 mL of 9 M HCl and stirred for 10 min. Afterward, 2 g Ti_3AlC_2 powders were slowly added to the etching solution and reacted at 35 °C for 24 h with continuous stirring. Subsequently, the product was repeatedly washed with deionized water and centrifuged at 3500 rpm ($1369.4 \times g$) for 10 min until the pH of the supernatant was above 5. To obtain mono/few-layer $Ti_3C_2T_x$, the black precipitate was redispersed in a mixed ethanol solvent and deionized water (1:1) and ultrasonically exfoliated for 1 h in an ice-water bath. The final exfoliated $Ti_3C_2T_x$ dispersion was obtained after removing ethanol, and the concentration was determined by filtration and vacuum drying.

Fabrication and assembly of a multimodal sensing unit (HM-S)

In a typical process, 10 g PVA was initially dissolved in 90 ml DI water at 85 °C, followed by adding 10 mg/ml mono/few-layer $Ti_3C_2T_x$ dispersion and vigorously stirring in an ice water bath for 10 min. The weight content of $Ti_3C_2T_x$ nanosheets in PVA was controlled at 0, 0.02, 0.04, 0.06, and 0.08, denoted as HM-0, HM-1, HM-2, HM-3, and HM-4, respectively. Afterward, 1 wt% sodium tetraborate solution was slowly mixed with the above dispersion to obtain PVA/MXene hydrogel. After being immersed in equivalent deionized water for 24 h, PVA/MXene hydrogel was transformed into a solution and poured into a PDMS-based microneedle mold. In order to eliminate micro-holes and construct directional alignment of nanosheets, PVA/MXene solution with mold was placed in a vacuum tank for at least three cycles of vacuum-refilling. Eventually, PVA/MXene composite hydrogel microneedle arrays were fabricated by curing the solution at 35 °C for 6 h. To enhance interfacial adhesiveness and construct NFJ between HM and ITO, PVA/MXene gel solution with the same content (4 % MXene) was coated on the PET/ITO (or Cu electrode) film first. The HM-2 unit ($1\,\mathrm{cm^2}$) was attached to the coating. Then, HM-S was fabricated after PDMS encapsulation for output performance testing.

Integration of in-sensing and computing e-skin

Before the bonding between HM and ITO, the neuromorphic computing unit was prepared on PET/ITO film by sequential evaporation and deposition of Al_2O_3, Pt, and Ag via the E-beam method, and the thicknesses of which were 10 nm, 2 nm, and 40 nm, respectively. To separate the top (Ag) and bottom (ITO) electrodes, part of the ITO film was applied with insulating tape. After E-beam evaporation, the HM-2 unit was adhered to the PET/ITO film on the other side of the computing unit, and then the hydrogel microneedle was encapsulated by PDMS.

Data availability

The data of this study are available within the article and the Supplementary Information file. All raw data generated during the current

study are available from the corresponding author upon request. Source data are provided with this paper.

References

1. Kang, K., Kim, K., Baek, J., Lee, D. J. & Yu, K. J. Biomimic and bioinspired soft neuromorphic tactile sensory system. *Appl. Phys. Rev.* **11**, 021328 (2024).
2. Yang, T.-H. et al. Recent advances and opportunities of active materials for haptic technologies in virtual and augmented reality. *Adv. Funct. Mater.* **31**, 202008831 (2021).
3. Xu, C., Solomon, S. A. & Gao, W. Artificial intelligence-powered electronic skin. *Nat. Mach. Intell.* **5**, 1344–1355 (2023).
4. Dai, Y., Hu, H., Wang, M., Xu, J. & Wang, S. Stretchable transistors and functional circuits for human-integrated electronics. *Nat. Electron.* **4**, 17–29 (2021).
5. Zhao, C., Park, J., Root, S. E. & Bao, Z. Skin-inspired soft bioelectronic materials, devices and systems. *Nat. Rev. Bioeng.* **2**, 671–690 (2024).
6. Dobashi, Y. et al. Piezoionic mechanoreceptors: Force-induced current generation in hydrogels. *Science* **376**, 502–507 (2022).
7. Fu, X., Cheng, W., Wan, G., Yang, Z. & Tee, B. C. K. Toward an AI era: Advances in electronic skins. *Chem. Rev.* **124**, 9899–9948 (2024).
8. Yang, C. & Suo, Z. Hydrogel ionotronics. *Nat. Rev. Mater.* **3**, 125–142 (2018).
9. Chen, B. et al. Giant negative thermopower of ionic hydrogel by synergistic coordination and hydration interactions. *Sci. Adv.* **7**, eabi723 (2021).
10. Wang, Y., Jia, K. & Suo, Z. Non-faradaic junction sensing. *Nat. Rev. Mater.* **10**, 176–190 (2024).
11. Kim, H. J., Chen, B., Suo, Z. & Hayward, R. C. Ionoelastomer junctions between polymer networks of fixed anions and cations. *Science* **367**, 773–776 (2020).
12. Warren, P. B. Non-faradaic electric currents in the Nernst-Planck equations and nonlocal diffusiophoresis of suspended colloids in crossed salt gradients. *Phys. Rev. Lett.* **124**, 248004 (2020).
13. Gittleson, F. S. & El Gabaly, F. Non-faradaic Li$^+$ migration and chemical coordination across solid-state battery interfaces. *Nano Lett.* **17**, 6974–6982 (2017).
14. Zhang, Y. et al. Hydrogel ionic diodes toward harvesting ultralow-frequency mechanical energy. *Adv. Mater.* **33**, 2103056 (2021).
15. Tadmor, R., Hernández-Zapata, E., Chen, N., Pincus, P. & Israelachvili, J. N. Debye length and double-layer forces in polyelectrolyte solutions. *Macromolecules* **35**, 2380–2388 (2002).
16. Zhang, Y.-Z. et al. MXene hydrogels: Fundamentals and applications. *Chem. Soc. Rev.* **49**, 7229–7251 (2020).
17. VahidMohammadi, A., Rosen, J. & Gogotsi, Y. The world of two-dimensional carbides and nitrides (MXenes). *Science* **372**, eabf158 (2021).
18. Xia, H. et al. Electricity generated by upstream proton diffusion in two-dimensional nanochannels. *Nat. Nanotechnol.* **19**, 1316–1322 (2024).
19. Mei, T. et al. Bio-inspired two-dimensional nanofluidic ionic transistor for neuromorphic. *Signal Process. Angew. Chem. Int. Ed.* **63**, e202401477 (2024).
20. Xie, L. et al. Ultrasensitive wearable pressure sensors with stress-concentrated tip-array design for long-term bimodal identification. *Adv. Mater.* **36**, 2406235 (2024).
21. Hu, L. et al. Hydrogel-based flexible electronics. *Adv. Mater.* **35**, 220532 (2023).
22. Kwon, H. -j et al. On-demand drug delivery bioelectronics through water-processable low dimensional high conductive MXene layer. *Lab Chip* **24**, 32943304 (2024).
23. Maksimovic, S. et al. Epidermal Merkel cells are mechanosensory cells that tune mammalian touch receptors. *Nature* **509**, 617–621 (2014).
24. Handler, A. & Ginty, D. D. The mechanosensory neurons of touch and their mechanisms of activation. *Nat. Rev. Neurosci.* **22**, 521–537 (2021).
25. Ma, G. et al. Bioinspired, fiber-based, flexible self-powered sensor for wearable applications. *Device* **2**, 100508 (2024).
26. Zou, Y., Xu, J., Chen, K. & Chen, J. Advances in nanostructures for high-performance triboelectric nanogenerators. *Adv. Mater. Technol.* **6**, 2000916 (2021).
27. Lin, L. et al. Triboelectric active sensor array for self-powered static and dynamic pressure detection and tactile imaging. *ACS Nano* **7**, 8266–8274 (2013).
28. Maksimenko, I. & Wellmann, P. J. Low-temperature processing of transparent conductive indium tin oxide nanocomposites using polyvinyl derivatives. *Thin Solid Films* **520**, 1341–1347 (2011).
29. Ruth, S. R. A., Feig, V. R., Tran, H. & Bao, Z. Microengineering pressure sensor active layers for improved performance. *Adv. Funct. Mater.* **30**, 2003491 (2020).
30. Xiao, B. Mechanisms of mechanotransduction and physiological roles of PIEZO channels. *Nat. Rev. Mol. Cell Biol.* **25**, 886–903 (2024).
31. Miyake, T. & Rolandi, M. Grotthuss mechanisms: From proton transport in proton wires to bioprotonic devices. *J. Phys. Condens Matter* **28**, 02300 (2016).
32. Qi, J. et al. Emerging two-dimensional materials for proton-based energy storage. *ACS Nano* **18**, 25910–25929 (2024).
33. Kim, H. et al. Organic mixed ionic-electronic conductors for bioelectronic sensors: materials and operation mechanisms. *Adv. Sci.* **11**, 230619 (2024).
34. Paulsen, B. D., Fabiano, S. & Rivnay, J. Mixed ionic-electronic transport in polymers. *Annu. Rev. Mater. Res.* **51**, 73–99 (2021).
35. Ho, D. The piezoionic effect: Biomimetic transduction mechanism for sensing, actuation, interface, and energy harvesting. *ChemElectroChem* **11**, e202300268 (2024).
36. Jin, C. et al. A superhuman sensing triboelectric nanogenerator with boosted power density and durability via a bio-inspired janus structure. *Adv. Funct. Mater.* **34**, 2402233 (2024).
37. Zhang, Y. et al. Highly stable flexible pressure sensors with a quasi-homogeneous composition and interlinked interfaces. *Nat. Commun.* **13**, 131 (2022).
38. Kim, Y., Kim, K. J., Kim, S. H. & Choi, J. Unveiling ion dynamics in the electric-double layer under piezoionic actuation of chemomechanical energy harvesters. *Adv. Energy Mater.* **14**, 2402216 (2024).
39. Donati, E. & Valle, G. Neuromorphic hardware for somatosensory neuroprostheses. *Nat. Commun.* **15**, 556 (2024).
40. Zidan, M. A., Strachan, J. P. & Lu, W. D. The future of electronics based on memristive systems. *Nat. Electron.* **1**, 22–29 (2018).
41. Yan, X. et al. Memristor with Ag-cluster-doped TiO$_2$ films as artificial synapse for neuroinspired computing. *Adv. Funct. Mater.* **28**, 1705320 (2018).
42. Chekol, S. A., Menzel, S., Ahmad, R. W., Waser, R. & Hoffmann-Eifert, S. Effect of the threshold kinetics on the filament relaxation behavior of Ag-based diffusive memristors. *Adv. Funct. Mater.* **32**, 2111242 (2022).
43. Wang, R. et al. High-performance Ta$_2$O$_5$-based resistive random-access memory with embedded graphene quantum dots and Pt-Ag composite active layer. *Appl. Phys. Lett.* **123**, 043502 (2023).
44. Li, H. et al. A bioinspired tactile scanner for computer haptics. *Nat. Commun.* **15**, 7632 (2024).
45. Chun, S. et al. An artificial neural tactile sensing system. *Nat. Electron.* **4**, 429438 (2021).
46. Zhao, S., Zhang, B., Yang, J., Zhou, J. & Xu, Y. Linear discriminant analysis. *Nat. Rev. Methods Prim.* **4**, 70 (2024).
47. Tan, H. et al. Tactile sensory coding and learning with bio-inspired optoelectronic spiking afferent nerves. *Nat. Commun.* **11**, 136 (2020).

Author contributions

M.D., P.X., and J.C.H. structured and designed the experiments. M.D., P.X., and J.W. performed the fabrication and characterization of hydrogel microneedles and devices. J.W. and M.D. finished the simulation of the devices. W.G., H.L., S.H., D.L., B.L., and N.W. helped with electrical measurements. M.D., P.X., J.W., W.G., and C.Y.W. analyzed the data. M.D., P.X., J.W., J.S., and J.C.H. co-wrote the paper. All authors discussed the results and commented on the manuscript.

Competing interests

The authors declare no competing interests.

Additional information

Supplementary information The online version contains supplementary material available at https://doi.org/10.1038/s41467-025-63115-9.

Correspondence and requests for materials should be addressed to Jia Sun or Johnny C. Ho.

Publisher's note Springer Nature remains neutral with regard to jurisdictional claims in published maps and institutional affiliations.